



Optimising NDWI supraglacial pond classification on Himalayan debris-covered glaciers

C. Scott Watson^{a,b,*}, Owen King^b, Evan S. Miles^b, Duncan J. Quincey^b

^a Department of Hydrology & Atmospheric Sciences, University of Arizona, Tucson, USA

^b School of Geography and water@leeds, University of Leeds, Leeds LS2 9JT, UK

ARTICLE INFO

Keywords:

Supraglacial ponds
Debris-covered glaciers
Sentinel-2
Normalised difference water index
Glacial lakes

ABSTRACT

The ability of medium-resolution (10–30 m) satellite imagery to delineate the size and persistence of ponds on debris-covered glaciers is a topic of recent interest as it has become apparent through the use of fine-resolution products that smaller ponds have often been neglected. In this study, we performed a quantitative analysis of pond detection using a normalised difference water index (NDWI) applied to several widely used satellite sensors, which offer multispectral information at high radiometric precision. These data include: RapidEye (5 m spatial resolution), Sentinel-2 Multispectral Instrument (MSI) (10–20 m), and Landsat 8 Operational Land Imager (OLI) multispectral imagery (30 m). We demonstrate a method to derive an optimum NDWI value for pond classification using a subset reference dataset of 285 ponds classified using fine-resolution (0.5 m) imagery. We then applied the optimised NDWI (NDWI-O) to the remaining images to assess pond classification accuracy against a broader reference dataset of 898 ponds. NDWI values calculated using Sentinel-2 imagery showed the best spectral contrast between water and surrounding debris cover, and the strongest relationship with pixel water content ($R^2 = 0.56$), followed by the RapidEye NDWI ($R^2 = 0.45$). We conclude that RapidEye and Sentinel-2 imagery is best suited for accurate pond classification using a multispectral classification approach, which is important for quantifying their role in glacier ablation, meltwater regulation, and lake development. By comparison, the impact of using coarse-resolution Landsat 8 imagery to characterise surface water dynamics is minimised when applied to large glacier lakes, where the area-to-perimeter ratio is greater.

1. Introduction

Supraglacial ponds can coalesce on low-gradient, stagnating debris-covered glaciers to form large proglacial lakes (Reynolds, 2000; Quincey et al., 2007; Benn et al., 2012). Proglacial lake development is a concern due to the risk of potential glacial lake outburst floods (GLOFs) (Worni et al., 2014; Rounce et al., 2017), and because accelerated ice loss occurs when lakes in contact with a glacier terminus (Sakai et al., 2009; Benn et al., 2012; Carrivick and Tweed, 2013). The accurate classification of supraglacial ponds is required to reveal decadal, multi-annual, and seasonal changes in pond area, and to determine the onset of a trajectory towards proglacial lake development. Additionally, studies have shown that supraglacial ponds are often associated with ice cliffs where they promote thermo-erosional undercutting and ice-cliff retreat (Sakai et al., 2009; Buri et al., 2016; Thompson et al., 2016; Miles E et al., 2017; Watson et al., 2017b, c). This pond-cliff interaction is correlated with high rates of surface lowering on debris-covered glaciers (e.g. Immerzeel et al., 2014;

Ragetti et al., 2016; Thompson et al., 2016; Watson et al., 2017a), leading to a positive feedback that promotes further ponding and ultimately glacial lake formation (Benn et al., 2012). Ponds regulate glacier runoff (Irvine-Fynn et al., 2017) and draining ponds can also contribute to internal ablation via thermal erosion (Miles et al., 2016a; Thompson et al., 2016; Miles E et al., 2017; Watson et al., 2017b). However, the contribution of surface and englacial hydrological processes to the glacier ablation budget remains relatively unknown.

Studies quantifying supraglacial pond and proglacial lake dynamics have typically exploited the long temporal archive of Landsat satellite imagery to classify water bodies using the normalised difference water index (NDWI) or object-based image analysis (OBIA) (McFeeters, 1996; Huggel et al., 2002; Gardelle et al., 2011; Liu et al., 2015; Miles et al., 2016b; Narama et al., 2017). However, the impact of image resolution on pond classification accuracy has only been investigated theoretically (e.g. Salerno et al., 2012), or using knowledge of pond size distributions derived from fine-resolution satellite imagery (e.g. Miles et al., 2016b; Watson et al., 2016). Watson et al. (2016) revealed that classification

* Corresponding author at: Department of Hydrology & Atmospheric Sciences, University of Arizona, Tucson, USA.

E-mail address: scott@rockyglaciers.co.uk (C.S. Watson).

omissions of pond area on the order of 15–88% could occur when using medium-resolution imagery (e.g. 30 m Landsat 8), compared to fine-resolution (e.g. 0.5 m) imagery. The NDWI value used to produce a binary classification of water vs. non-water is most often derived by visual inspection (e.g. Gardelle et al., 2011; Miles et al., 2016b; Miles K et al., 2017), and the sensitivity of this value can only be evaluated with a fine-resolution reference dataset (Ji et al., 2009) or using pond perimeters from field data. Therefore, due to the irregularity of supraglacial ponds' shorelines, the classification of such ponds using medium-resolution imagery requires consideration of two major issues: (1) mixed pixels along the shoreline comprising both water and debris cover, which could be assigned to either class based on a user-defined NDWI value; and (2) the omission of ponds smaller than a minimum areal threshold, which is at least one pixel but potentially at least four pixels to ensure robust pond identification (Gardelle et al., 2011).

In this study, we quantify the relationship between the NDWI classification accuracy of supraglacial ponds and the resolution of the satellite imagery used. Specifically we: (1) demonstrate a method to optimise NDWI pond classification with RapidEye, Sentinel-2, and Landsat 8 imagery using a calibration dataset derived from fine-resolution imagery; (2) quantify the relationship between pixel water content and an NDWI applied to RapidEye, Sentinel-2, and Landsat 8 imagery; (3) quantify the omissions and commissions of supraglacial ponds expected when using the NDWI to classify ponds on satellite imagery of different resolution; and (4) discuss the optimum scenarios for supraglacial pond classification.

2. Study area and data

We focus our study on eight debris-covered glaciers in the Everest region of Nepal (Fig. 1). The glaciers have exhibited a negative mass balance in recent years (Benn et al., 2012; King et al., 2017) due to warming temperatures and reduced precipitation (Shrestha and Aryal,

2011; Salerno et al., 2015). Mass loss is leading to glacier stagnation (Quincey et al., 2009; Watson and King, 2018) and increased but variable supraglacial water storage, both across glaciers and through time (Watson et al., 2016). Supraglacial ponds form on the debris-covered ablation zones and often expand during the melt season until they establish an efficient englacial connection (Benn et al., 2012; Miles et al., 2016b, Miles E et al., 2017; Watson et al., 2017b).

We first analyse a set of imagery acquired during November 2016 with a maximum time separation of 16 days (Table 1). To assess reproducibility, we then applied the same methods to an imagery set from 2017, which was acquired in November and December 2017, with a maximum time separation of 19 days. Winter images are generally cloud-free, in contrast to those acquired during the Indian Summer Monsoon. We assumed each image captured the same distribution of ponds in these winter months (e.g. Fig. 2), since ponds are most dynamic during the summer melt season (Miles et al., 2016b; Watson et al., 2017b). The surface of these lakes is also likely to be freezing over during these months (Watson et al., 2017b). We excluded the large lake present on Changri Nup Glacier from our analysis due to prevalent shadows in the imagery, which can cause erroneous classification under the NDWI approach (e.g. Miles et al., 2016b).

3. Methods

3.1. Imagery pre-processing and NDWI generation

All satellite imagery was captured during clear-sky conditions. The panchromatic Pléiades image was captured as a stereo pair by the Pléiades-1A satellite and was orthorectified in the ERDAS IMAGINE Leica Photogrammetry Suite with a DEM generated from the stereo imagery. RapidEye imagery was processed to surface reflectance using the GRASS GIS i.atcorr tool, which uses the 6S radiative transfer algorithm (Vermote et al., 1997; Kotchenova et al., 2006; Kotchenova and

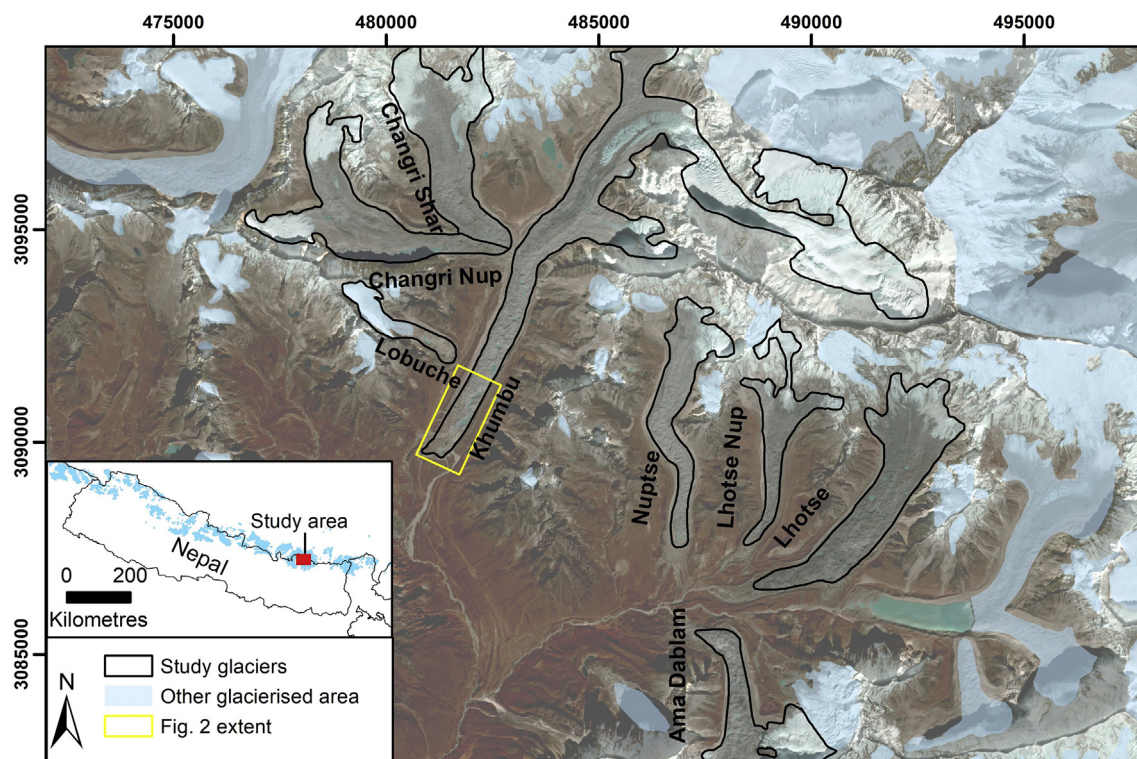


Fig. 1. Study glaciers in the Everest region of Nepal. Glacier outlines were modified from the Randolph Glacier Inventory 6.0 (RGI Consortium, 2017) to separate Changri Nup and Changri Shar glaciers and to add omitted debris-covered areas of Lobuche and Khumbu Glaciers. Backdrop: Sentinel-2 false-colour composite (NIR, green, and blue) 29th November 2016. Grid: UTM 45 N. (For interpretation of the references to colour in this figure legend, the reader is referred to the web version of this article.)

Table 1
Everest region satellite imagery.

Imagery set	Source	Acquisition date and time (Nepal)	Spatial resolution	Purpose
2016	Pléiades-1A panchromatic image	13th November 2016, 10:46 AM	0.5 m	Derive a fine-resolution reference pond dataset
	RapidEye multispectral imagery	17th November 2016, 11:07 AM	5 m	Investigate the relationship between NDWI and the reference pond dataset
	Sentinel-2 multispectral imagery	29th November 2016, 10:37 AM	10 m near-infrared (NIR) 20 m short-wavelength infrared (SWIR)	Investigate the relationship between NDWI and the reference pond dataset
2017	Landsat 8 multispectral imagery	19th November 2016, 10:28 AM	30 m	Investigate the relationship between NDWI and the reference pond dataset
	PlanetScope multispectral imagery	19th November 2017, 09:56 AM	3 m	Derive a fine-resolution reference pond dataset
	RapidEye multispectral imagery	19th November 2017, 11:03 AM	5 m	Investigate the relationship between NDWI and the reference pond dataset
	Sentinel-2 multispectral imagery	24th November 2017, 10:49 AM	10 m NIR	Investigate the relationship between NDWI and the reference pond dataset
	Landsat 8 multispectral imagery	8th December 2017, 10:27 AM	30 m	Investigate the relationship between NDWI and the reference pond dataset

All sensors have 12-bit radiometric resolution.

Vermote, 2007). We input the ASTER GDEM2 and the RapidEye metadata supplied by Planet Labs (Planet Team, 2017). The default RapidEye parameters were used to process the blue and red bands; however, these produced an erroneous result for the green and NIR bands. We therefore used Landsat 7 Enhanced Thematic Mapper Plus (ETM+) parameters, which were of similar spectral characteristics in the green and NIR bands (Chander et al., 2013). We used the midlatitude winter atmospheric model and continental aerosol model. The only constituent specified was aerosol optical depth, which was derived from Moderate Resolution Imaging Spectroradiometer monthly data interpolated to the image centre (NASA Earth Observations, 2018). The Sentinel-2 imagery was delivered as a Level-2A (atmospherically corrected bottom-of-atmosphere product) surface reflectance product from the data service platform implemented by the University of Natural Resources and Life Science, BOKU (Vuolo et al., 2016). The Landsat 8 imagery was delivered as a surface reflectance product from the USGS Earth Resources Observation and Science (EROS) Center Science Processing Architecture (ESPA) On Demand Interface.

NDWI images were derived using combinations of the NIR and green bands (e.g. Gardelle et al., 2011; Nie et al., 2013) and SWIR and green bands (Eqs. (1)–(4)). SWIR bands were used for Sentinel-2 and Landsat 8 since studies have shown improved water classification compared to the NIR band (Ji et al., 2009; Li et al., 2013; Du et al., 2014). The NIR band of Sentinel-2 was acquired at 10 m resolution, whereas the SWIR band is 20 m resolution, therefore we derived two NDWIs for the Sentinel-2 product hereafter referred to as Sentinel-2_{NIR} and Sentinel-2_{SWIR}.

$$\text{RapidEye} = \frac{(\text{Band } 5_{\text{NIR}} - \text{Band } 2_{\text{Green}})}{(\text{Band } 5_{\text{NIR}} + \text{Band } 2_{\text{Green}})} \quad (1)$$

$$\text{Sentinel-2}_{\text{NIR}} = \frac{(\text{Band } 8_{\text{NIR}} - \text{Band } 3_{\text{Green}})}{(\text{Band } 8_{\text{NIR}} + \text{Band } 3_{\text{Green}})} \quad (2)$$

$$\text{Sentinel-2}_{\text{SWIR}} = \frac{(\text{Band } 11_{\text{SWIR}} - \text{Band } 3_{\text{Green}})}{(\text{Band } 11_{\text{SWIR}} + \text{Band } 3_{\text{Green}})} \quad (3)$$

$$\text{Landsat} = \frac{(\text{Band } 6_{\text{SWIR}} - \text{Band } 3_{\text{Green}})}{(\text{Band } 6_{\text{SWIR}} + \text{Band } 3_{\text{Green}})} \quad (4)$$

3.2. Reference pond datasets

To derive the 2016 reference pond dataset, supraglacial ponds were semi-automatically classified on all study glaciers using the orthorectified panchromatic Pléiades image and OBIA following Watson et al. (2016). Here, the panchromatic band was segmented and the polygons were exported. Pond polygons were extracted manually from the segmentation with supplementary reference to the multispectral RapidEye image. Pond boundaries were manually corrected where required (e.g. in areas of shadow beneath ice cliffs), or manually digitised if they were not accurately segmented. The reference pond dataset for the 2017 imagery set was derived using a NDWI (NIR and green bands) applied to a 3 m resolution PlanetScope image. Ponds were extracted using a user-defined threshold and manually inspected and corrected similar to the 2016 reference dataset.

A ± 0.5 pixel buffer applied to pond or lake boundaries is commonly used for uncertainty assessments (Fujita et al., 2009; Salerno et al., 2012). However, since our analysis assumed coincident imagery acquisition, which was not the case, we opted to use one-pixel buffers to represent uncertainty in our reference datasets to account for potential pond expansion or contraction between the acquisitions.

3.3. NDWI calibration and pond classification

We present a method that uses a reference dataset of supraglacial ponds on Khumbu Glacier to optimise NDWI values that are used to produce a binary classification of ponds. This method derives the NDWI

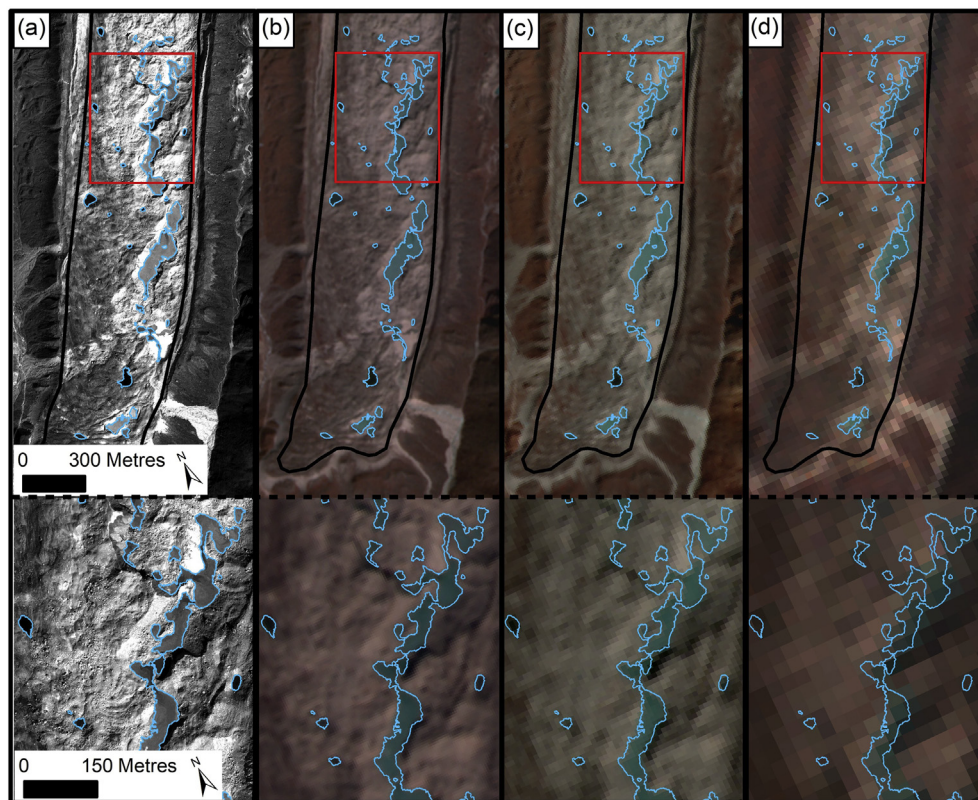


Fig. 2. The lower terminus of Khumbu Glacier shown with the satellite imagery products used in this study. (a) Pléiades panchromatic image with classified supraglacial ponds outlined in blue derived through OBIA following [Watson et al. \(2016\)](#). (b) RapidEye FCC (NIR, green, and blue). (c) Sentinel-2 FCC (NIR, green, and blue). (d) Landsat 8 FCC (NIR, green, and blue). Red boxes in the top panels are shown with magnification in the bottom panels for visualisation purposes. (For interpretation of the references to colour in this figure legend, the reader is referred to the web version of this article.)

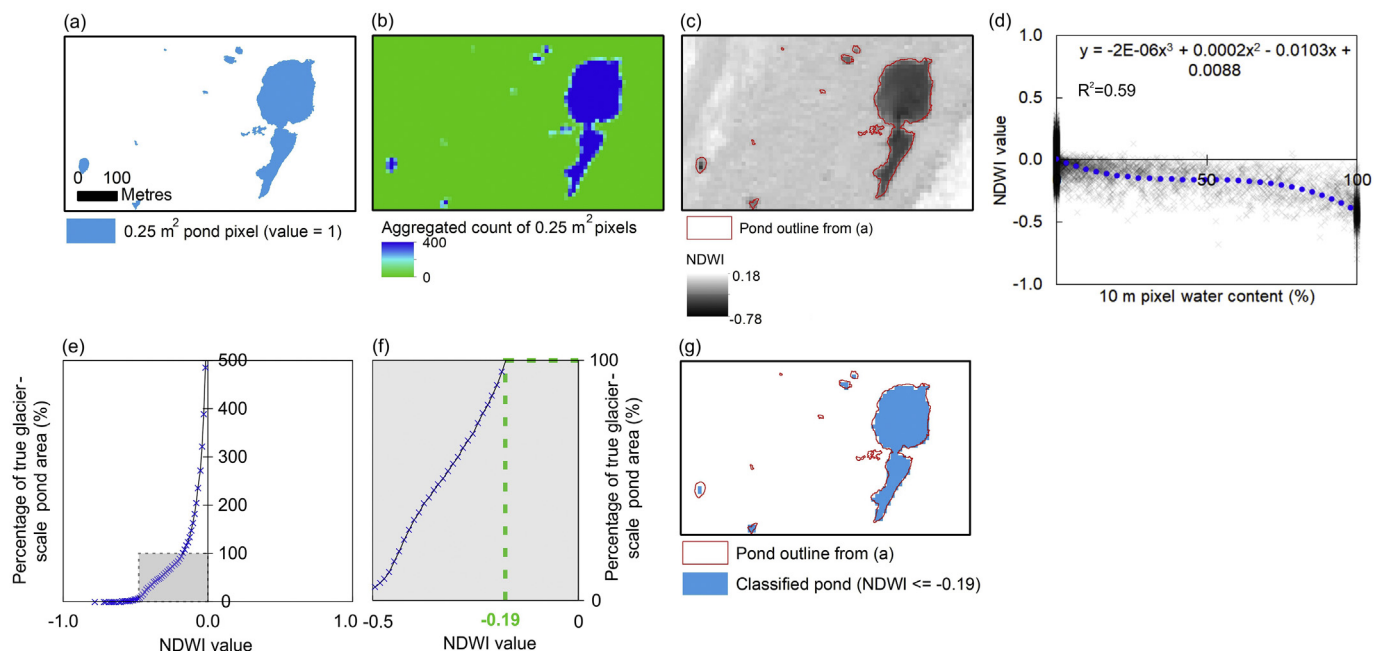


Fig. 3. Calibration of the NDWI using a fine-resolution (Pléiades) pond dataset (a). (b) The rasterised ponds were aggregated to the required sensor resolution (e.g. 10 m for Sentinel-2). Here, the maximum number of 0.25 m² pixels within the aggregated 100 m² pixel is 400, which represents 100% pixel water content. The maximum value would be 100 for RapidEye or 3600 for Landsat. (c) NDWI derived from the Sentinel-2 NIR and green bands. (d) The relationship between the aggregated pixel water content and the Sentinel-2 NDWI values with a 3rd order polynomial fit. (e) The area of pixels was cumulatively summed for an increasing NDWI value, which is used to derive the NDWI-O value (f) that provides the correct glacier-scale pond area for Khumbu Glacier known from the reference dataset (192,412 m²). (g) The NDWI-O was applied to the NDWI in (c), to produce a binary classification of ponds.

value, which we term the optimised NDWI value (NDWI-O), which is necessary to correctly account for the total pond area of the reference dataset. The NDWI-O is then applied to the whole satellite image to classify ponds on all study glaciers. Here we hypothesise that ponds on

Khumbu Glacier, which vary in size and turbidity, are sufficient to characterise an NDWI-O that can be used to classify all other ponds in the satellite image. The method follows a seven-step process ([Fig. 3a–g](#)) and is semi-automated within the GIS environment. Data export and

user intervention is required at (e) to derive the optimum NDWI value:

- A fine-resolution pond dataset was created over the region of interest and rasterised. This is referred to as the reference dataset and provides the total glacier-scale pond area for each study glacier. In this study we derived the reference pond dataset (Section 3.2) for all study glaciers to quantitatively assess the optimised NDWI performance; however, we only used ponds on Khumbu Glacier (number = 285) to derive the NDWI-O.
- The raster pond data were aggregated by summation to the pixel resolution of the image to be calibrated (e.g. 10 m for the Sentinel-2_{NIR}), which was carried out using the Aggregate tool in ArcGIS.
- The NDWI was calculated using a band ratio (e.g. Eqs. (1)–(4)).
- The number of water-covered pixels as defined by the reference dataset within the aggregated pixels is known from (b). This was converted to the percentage water content of each pixel. All on-glacier pixels in (b) and (c) were sampled to derive the relationship between pixel water content and the NDWI. However, this step is not required to derive the NDWI-O.
- The total area of all reference ponds on Khumbu Glacier (glacier-scale pond area) was used to find the NDWI value that would produce a binary classification with an area equal to 100% of the reference glacier-scale pond area (NDWI-O).
- In this process, the area of pixels is cumulatively summed for an increasing NDWI value (i.e. progressively lower water content), until the area of pixels equals the glacier-scale pond area.
- The NDWI-O is applied across the whole image to produce a binary classification of supraglacial ponds, which were clipped to the debris-covered area of the study glaciers and compared to the reference dataset. No manual corrections were applied to the NDWI-O derived ponds.

We used masks corresponding to the reference pond dataset and the debris-covered area of all study glaciers to sample each NDWI output (Eqs. (1)–(4)). These statistics quantified the range of NDWI values encountered for ponds and debris, and hence the spectral separation between the two feature classes (Fig. 4b). We also investigated the relationship between NDWI outputs and the blue index, which is a proxy for pond turbidity (Kraaijenbrink et al., 2016). The blue index was calculated for RapidEye, Sentinel-2 and Landsat 8 imagery using the band ratio:

$$\text{Blue index (BI)} = \frac{\text{Blue}}{\text{Red} + \text{Green}} \quad (5)$$

A low BI indicates ponds with a higher suspended sediment concentration, whereas a high BI indicates bluer ponds with a lower suspended sediment concentration (Kraaijenbrink et al., 2016).

4. Results

The 2016 reference pond dataset derived from the Pléiades image comprised 898 supraglacial ponds across the eight study glaciers. Ponds ranged in size from 3 to 28,179 m², with a mean size of 563 m² (one standard deviation of 1954 m²). Ponds ≤ 300 m² represented 72% of the total number of ponds and 12% of the total pond area (Fig. 4a). The 2017 reference pond dataset derived from a PlanetScope image comprised 623 ponds, with a range of 9–30,635 m² and a mean size of 654 m² (one standard deviation of 1967 m²).

4.1. Pixel water content and NDWI relationships

The size distribution of supraglacial ponds (Fig. 4a, Fig. S1) determines the performance of each sensor when resolving water pixels, such that a higher frequency of smaller ponds decreases the suitability of using coarser-resolution imagery for their classification (Salerno et al., 2012). NDWI values extracted for ponds and debris cover in 2016

revealed the range of NDWI values for each band ratio, and the spectral separation between these classes. The separation of median NDWI values for debris and ponds was 0.26 (RapidEye), 0.28 (Sentinel-2_{NIR}), 0.36 (Sentinel-2_{SWIR}), and 0.22 (Landsat 8) (Fig. 4b). Pond NDWI values for Sentinel-2_{SWIR} and Landsat 8 had the largest range of 1.3 and 1.4 respectively, compared to RapidEye and Sentinel-2_{NIR}, which had ranges of 0.9 and 1.1 respectively (Fig. 4b). Therefore, Sentinel-2_{SWIR} and Landsat 8 had the weakest relationships between NDWI values and pixel water content (Fig. 4e, f). By contrast, the relationship between NDWI and pixel water content was stronger for RapidEye and Sentinel-2_{NIR} ($R^2 = 0.45$ and 0.56 respectively, $p < 0.05$) (Fig. 4c, d). Since Sentinel-2_{NIR} performed better than Sentinel-2_{SWIR}, we only applied the NDWI optimisation to the former.

4.2. NDWI-O classified ponds

The NDWI-Os derived using reference pond datasets on Khumbu Glacier, were applied to RapidEye, Sentinel-2_{SWIR}, Sentinel-2_{NIR} and Landsat 8 images to classify supraglacial ponds across the eight study glaciers. The classification of these ponds was evaluated against the 2016 and 2017 reference datasets. The derived relationship between pixel water content and the Sentinel-2_{NIR} NDWI for Khumbu Glacier (Fig. 3d) was similar to the relationship across all study glaciers (Fig. 4d). This supported the use of reference ponds on Khumbu Glacier for deriving NDWI-Os, which were then applied across all study glaciers.

In 2016, pond area delineated by the reference dataset was best classified by Sentinel-2_{NIR} for five glaciers, Landsat 8 for two, and RapidEye for one (Fig. 5a). By contrast, the number of ponds in the reference dataset was best derived using RapidEye, followed by Sentinel-2 and Landsat 8, with the notable exception of Ama Dablam Glacier (Fig. 5b). In 2017, the pond area delineated by the reference dataset was best classified by RapidEye for four glaciers, Sentinel-2_{NIR} for three, and Landsat 8 for one (Fig. 5c). The number of ponds were best derived with Sentinel-2_{NIR}, whereas RapidEye generally overestimated the number of ponds (Fig. 5d).

Comparisons of spatially coincident ponds for each NDWI-O (Fig. 6) revealed a stronger correlation for RapidEye ($R^2 = 0.98$, root-mean-square error (RMSE) = 424 m²) and Sentinel-2_{NIR} ($R^2 = 0.97$, RMSE = 446 m²), compared to Landsat 8 ($R^2 = 0.79$, RMSE = 2489 m²). All correlations were statistically significant ($p < 0.05$). Additionally, the area of ponds < ~5000 m² was poorly classified by Landsat 8 (Fig. 6c). The notable area underestimation of a reference pond (28,224 m²) by Landsat 8 (Fig. 6c) was the network of connected pond basins shown in the expanded insets of Fig. 2.

Our results show that the optimised NDWI-O performs better on some glaciers than others (Fig. 5). Additionally, the area and number of ponds was still generally underestimated for Landsat 8. These errors are related to the presence of omissions and commissions, which are discussed in the following section and are linked to the pond size distribution for each glacier. For example, ponds on Lobuche and Ama Dablam Glaciers tended to be larger than on other glaciers (Fig. S1), which corresponds with improved Landsat 8 classification of the number of ponds (Fig. 5b). The variable turbidity of ponds also likely exerts some influence over classification ability. However, we found no clear relationship between Blue index and NDWI values (Fig. S2), suggesting that pond turbidity is generally consistent across the study glaciers, although some outliers existed.

4.3. Omissions and commissions

The omissions and commissions reported in Table 2 represent a complete omission or commission, i.e. where a pond was present in the reference dataset but not in the NDWI dataset (omission), or where a pond was not present in the reference dataset but was falsely delineated in the NDWI dataset (commission). The commission of Landsat 8 pond

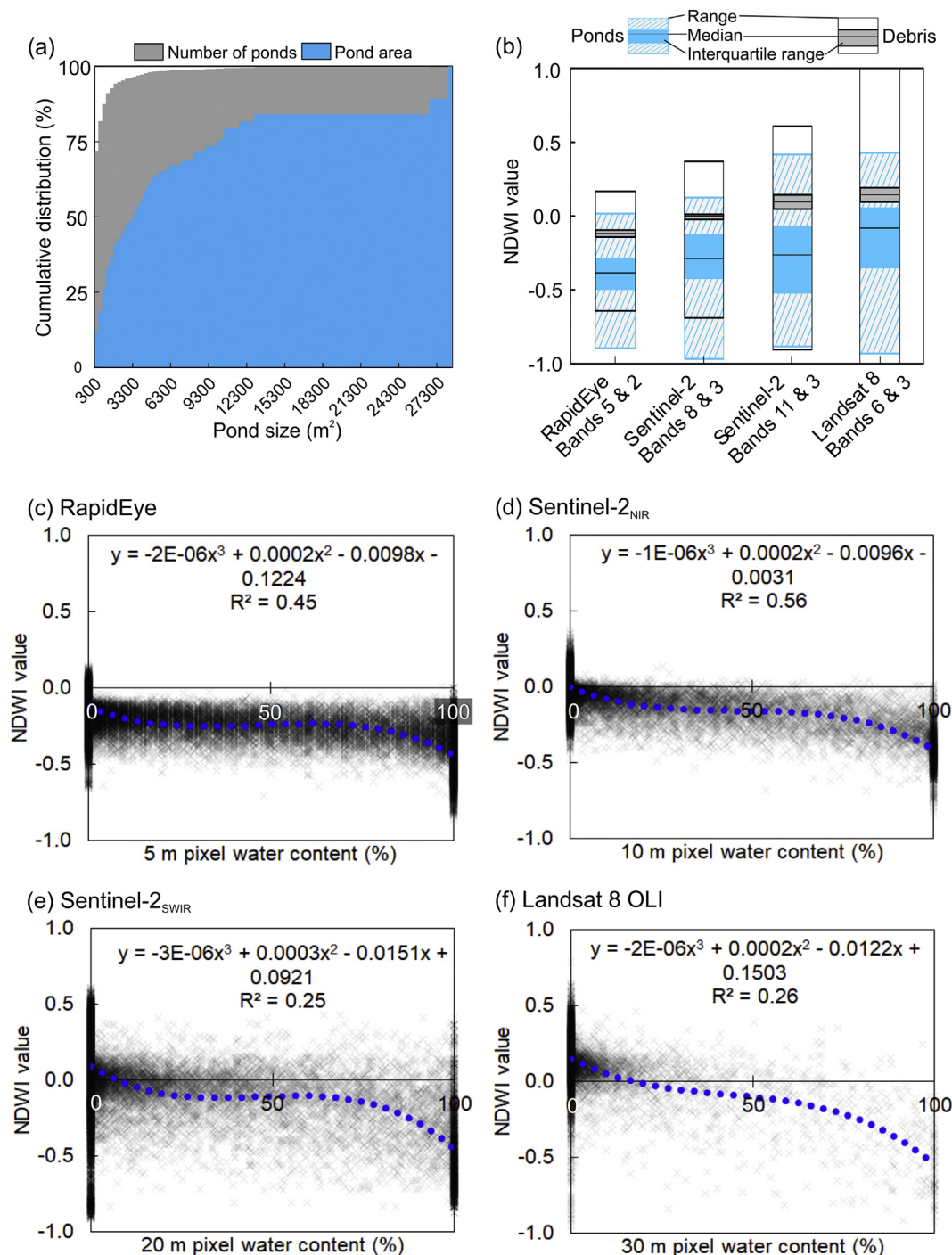


Fig. 4. (a) Cumulative distribution of pond area and number (300 m² bins) from the 2016 reference dataset. (b) NDWI values for ponds and debris-covered zones showing the median, interquartile range and data range for ponds and debris. (c–f) Relationship between pixel water content and NDWI values for RapidEye (c), Sentinel-2_{NIR} (d), Sentinel-2_{SWIR} (e), and Landsat 8 (f) respectively. 3rd order polynomial trends are fitted ($p < 0.05$).

area in 2016 was twice that of Sentinel-2_{NIR} and greater than RapidEye (Table 2). These trends were similar in 2017. Landsat 8 omissions were three times greater than Sentinel-2 and five times greater than RapidEye (Table 2). Again, the trends were similar in 2017.

The net difference between the total area of NDWI-O classified ponds and the 2016 reference dataset pond area was -1% for Sentinel-2_{NIR} and RapidEye, and -11% for Landsat 8 (Table 3). RapidEye produced the lowest net difference (-2%) in total pond number compared to the reference dataset. However, it is clear that commissions and omissions of individual ponds are large and partially offset each

other (Table 2) to produce a more accurate glacier-scale result, and that there is variability in the classification accuracy between glaciers. The theoretical omissions from using a sensor of specific pixel size can be approximated by quantifying the area and number of ponds falling below the area of one pixel for each sensor (Table 3). In 2016, ponds falling below the area of one pixel were $< 1\%$ of the total by number and area for RapidEye (25 m²) imagery (Table 3). By contrast, 87% and 26% of ponds by number and area respectively were below the size of one Landsat 8 pixel (900 m²), and 48% and 4% for Sentinel-2_{NIR} (100 m²). The omissions we observed during pond classification always

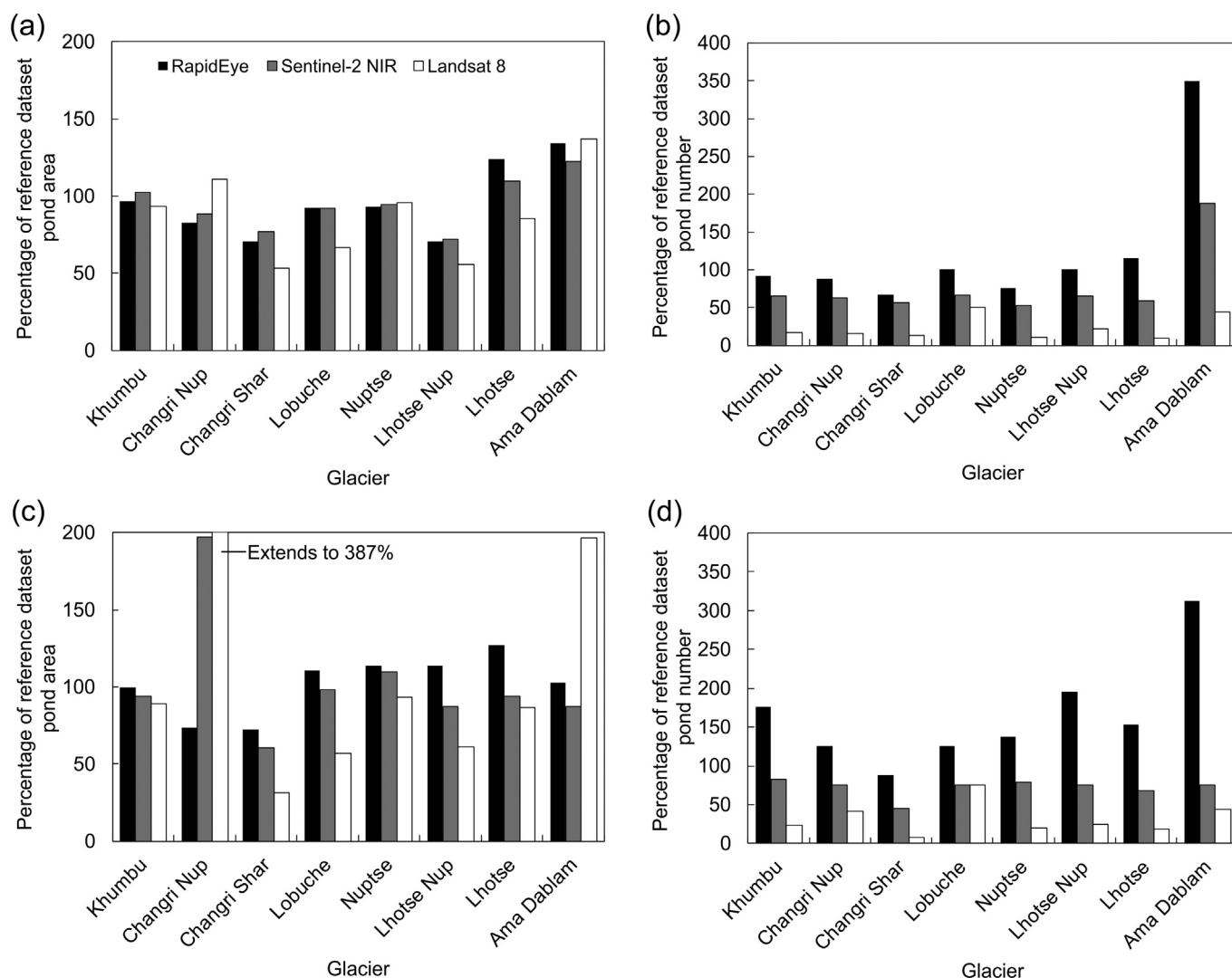


Fig. 5. The area and number of ponds delineated for each sensor as a percentage of the reference dataset in 2016 (a, b) and 2017 (c, d).

exceeded the theoretical omissions and were largest for Landsat 8, followed by Sentinel-2_{NIR} and RapidEye (Table 3). Notably, despite a theoretical pond number omission of < 1% for RapidEye, the actual omissions were 48% of the true number of ponds.

Classification accuracy was variable across glaciers (Fig. 5), and key features contributed to the observed omissions and commissions (Fig. 7). Omissions were prevalent in areas of small ponds, such as on Lhotse Glacier for Sentinel-2_{NIR} (Fig. 7b); however, omissions were widespread for Landsat 8. Supraglacial meltwater channels were notable areas of commission, especially for RapidEye and Sentinel-2_{NIR}, where the narrow channels are better resolved. Ice cliffs, which are predominantly northerly-facing (Watson et al., 2017a), caused notable commissions for RapidEye due to shadowing (Fig. 7a).

4.4. Classification sensitivity to NDWI values

NDWI values that delineated 80% and 120% of the true reference dataset pond area were derived to demonstrate the sensitivity of pond classification to the NDWI value used. Such variation around the optimum NDWI value could result from a user-defined value that was selected through manual inspection (Gardelle et al., 2011). Sentinel-2_{NIR} and Landsat 8 NDWI values displayed the same sensitivity to over- or under-estimation of glacier-scale pond area by $\pm 20\%$ in 2016;

however, NDWI values were variable in 2017 (Table 4). The larger uncertainty values in 2017 reflect the coarser resolution (3 m Planet-Scope) reference pond dataset, compared to the 0.5 m Pléiades imagery used in 2016.

5. Discussion

The accurate classification of supraglacial ponds on debris-covered glaciers is required to quantify their role towards meltwater generation and storage, and glacial lake development. However, the ability of different spatial resolution satellite imagery to discriminate ponds has received little attention.

Our reference datasets showed that supraglacial ponds are generally small, with ponds $\leq 300 \text{ m}^2$ representing 72% of the total number of ponds and 12% of the total pond area in 2016 (Fig. 4a). Similarly, the total pond area less than one Landsat 8 pixel (900 m^2) was 26%, which is in agreement with the range observed by Watson et al. (2016) (15–40%) on nine glaciers in the Everest region, including five of the glaciers featured in this study (Khumbu, Nuptse, Lhotse Nup, Lhotse, and Ama Dablam). In comparison, Miles et al. (2016b) observed that pond area less than one Landsat 8 pixel (900 m^2) was 7% of the total in the Langtang region, revealing that glacier pond size distributions are spatially variable between glaciers (Fig. S1), and regionally.

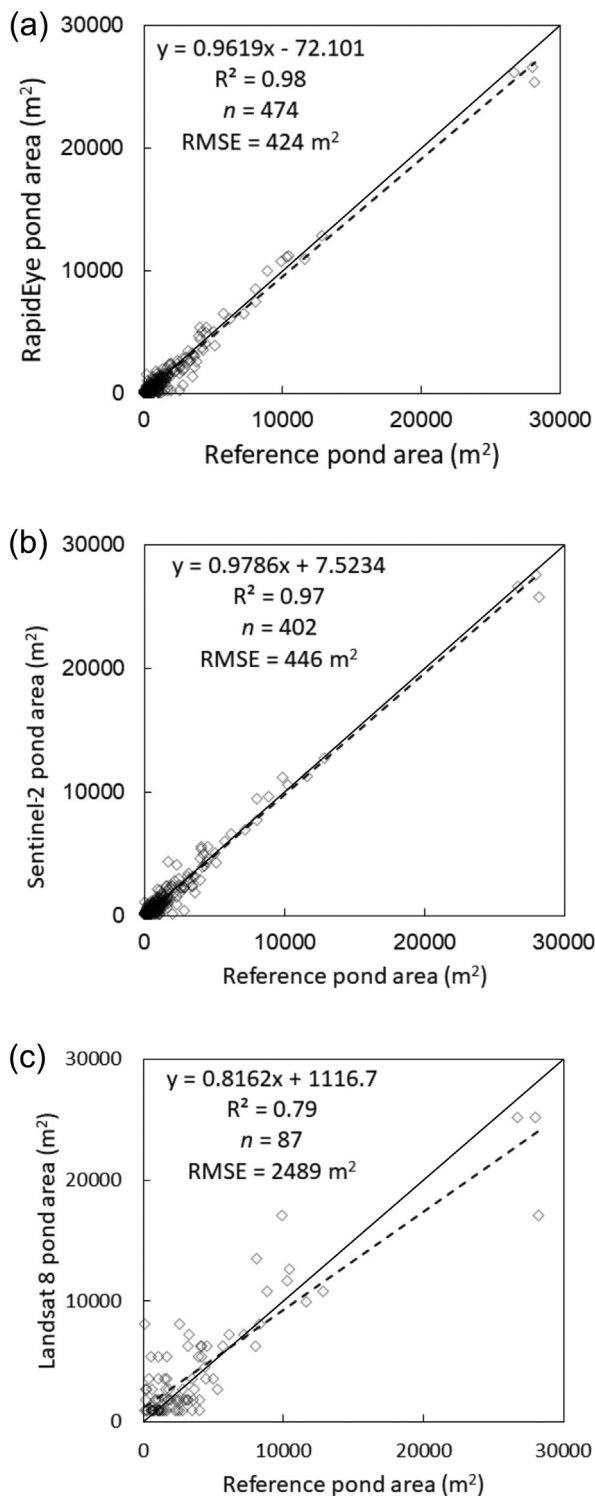


Fig. 6. Comparison of NDWI-O and reference pond areas in 2016 for (a) RapidEye, (b) Sentinel-2, and (c) Landsat 8. Ordinary least squares regressions lines are shown dashed ($p < 0.05$). Linear direct lines are solid black.

5.1. Pixel water content and NDWI relationships

We quantified the relationship between pixel water content, which was derived from the reference dataset, and NDWI values. Both RapidEye and Sentinel-2_{NIR} NDWI images featured good spectral separation of ponds and debris cover (Fig. 4b), and the strongest correlations between NDWI values and pixel water content (Fig. 4c, d). The

lower correlation for Sentinel-2_{SWIR} was likely because the NDWI was produced at the resolution of the green band (10 m), which oversampled the SWIR band (20 m) (Fig. 4e). Sentinel-2_{NIR} had a larger NDWI separation between ponds and debris cover compared to RapidEye imagery, and a stronger relationship with pixel water content (Sentinel-2_{NIR} $R^2 = 0.56$, RapidEye $R^2 = 0.45$) despite a larger pixel size. We expect that the variable off-nadir viewing angle of RapidEye acts to extenuate predominantly northerly-facing ice cliff shadows (e.g. Watson et al., 2017a), which were notable areas of commission (Fig. 7a). Notably, the NDWI values for ponds and debris overlap for all sensors (Fig. 4b), which highlights why the classification of ponds on debris-covered glaciers is a non-trivial task. The area of individual ponds delineated with the RapidEye and Sentinel-2_{NIR} NDWI-Os was strongly correlated with those of the reference pond dataset, and this relationship was closer to a linear direct fit than the Landsat 8 NDWI-O (Fig. 6).

5.2. Classification of supraglacial ponds

The large temporal archive and spatial coverage of Landsat imagery means that the product is already suitable for analysing long-term temporal trends in pond area (e.g. Gardelle et al., 2011; Miles et al., 2016b). However, the use of Sentinel-2 imagery is limited by its young age as a sufficient archive develops, although image acquisition increased towards the ends of 2017 with the launch of Sentinel-2B (Fig. 8). The finer resolution of RapidEye and Sentinel-2 imagery offers greater suitability for supraglacial pond classification compared to Landsat 8, owing to the prevalence of small ponds (Watson et al., 2016).

We observed high pond area classification accuracy across our study area, with a net difference between the total area of classified ponds and the 2016 reference dataset pond area of -1% for Sentinel-2_{NIR} and RapidEye, and -11% for Landsat 8 (Table 3). However, the classification accuracy was variable across glaciers (Figs. 5, 7), which reflects the balance of omissions and commissions and different pond size distributions across the study glaciers (cf. Watson et al., 2016, their Fig. 8 and our Fig. S1). Glaciers with a larger proportion of smaller ponds such as Lhotse Glacier featured poorer classification accuracy using Landsat 8, in contrast to those with larger ponds such as Lobuche and Ama Dablam Glaciers.

Omissions and commissions of pond area were 34% and 16% respectively for the 2016 Landsat 8 NDWI-O. Therefore, while Landsat 8 underestimated the total pond area on our study glaciers by 11%, the errors at the scale of individual ponds were greater. Commissions can offset omissions, leading to a more accurate prediction of the total pond area by virtue of these errors for all sensors (Table 2). However, the increased spatial resolution of RapidEye and Sentinel-2 leads to improved classification accuracy for both pond area and number. The area of individual ponds was also best resolved using RapidEye and Sentinel-2 with RMSEs of 424 m² and 446 m² respectively, compared to Landsat 8 (RMSE = 2489 m²) (Fig. 6).

5.3. Optimal classification of supraglacial ponds

Our results demonstrate that imagery $\leq 10 \text{ m}$ resolution is suitable for pond- and glacier-scale analyses such as deriving area-volume relationships (Watson et al., 2017b), assessing meltwater storage and transmission (Irvine-Fynn et al., 2017; Miles E et al., 2017), and quantifying the role of ponds as ‘hot spots’ of glacier melt (Thompson et al., 2016). By comparison, Landsat 8 NDWIs can be optimised to estimate regional water storage, but large omissions and commissions are present at glacier scales. Therefore, Landsat 8 imagery is better suited to mapping proglacial lakes where shoreline mixed pixels constitute a lower proportion of the total lake area (Gardelle et al., 2011; Nie et al., 2013).

Images approaching winter are often selected to quantify ponds at the end of the ablation season, however; pond mapping becomes more

Table 2
Omission and commission of supraglacial ponds.

		RapidEye commission	RapidEye omission	Sentinel-2 _{NIR} commission	Sentinel-2 _{NIR} omission	Landsat 8 commission	Landsat 8 omission
2016	Pond area (m ²)	56,000	33,706	32,300	48,727	80,100	173,435
	Number of ponds	379	428	128	497	36	796
2017	Pond area (m ²)	71,150	31,843	39,500	38,587	100,800	130,444
	Number of ponds	533	272	126	313	43	523

2016 total reference pond area = 507,642 m² and number = 898.

2017 total reference pond area = 423,692 m² and number = 663.

difficult when the surface begins to freeze (Miles et al., 2016b). We observed a stronger relationship ($R^2 = 0.40$) between NDWI and Landsat 8 pixel water content for an image acquired on 10th June 2015 (Figs. S3 and S4), compared to the November image ($R^2 = 0.26$) (Fig. 4f). This reflects fully thawed supraglacial ponds in June, compared to partially frozen ponds in November. Summer images are often unsuitable due to the prevalence of cloud cover during the monsoon (e.g. Fig. 8). However, the five-day revisit frequency of Sentinel-2 and near-daily temporal resolution offered by PlanetScope provides new opportunities to investigate cloud-free periods during the ablation season. Nonetheless, to analyse seasonal pond dynamics requires determination of an NDWI threshold without validation data (e.g. Miles et al., 2016b; Narama et al., 2017). Our results suggest that such analyses need to implement more advanced techniques to identify ponded water, such as spectral unmixing (Alcántara et al., 2009) or iterative histogram-based thresholding (Cooley et al., 2017) to reliably resolve supraglacial ponds. Additionally, future work could include an inter-comparison with other methods of optimised decision making such as the Receiver operating characteristics (ROC) analysis (Fawcett, 2006).

5.4. Broader relevance

Our method of optimising NDWI values is applicable across the Himalayas and to other regions containing debris-covered glaciers such as in Alaska or New Zealand, where the size of supraglacial ponds are the same order of magnitude as those in this study (Kirkbride, 1993; Rohl, 2008). By comparison, the larger size of supraglacial lakes on the Greenland Ice Sheet are suited to mapping with Landsat or coarser-resolution imagery (e.g. Sundal et al., 2009; Leeson et al., 2013; Miles K et al., 2017; Williamson et al., 2017). Additionally, the spectral heterogeneity of the debris-covered glacier surface makes finding the optimal NDWI value more difficult compared to a more distinct ice and water separation.

Table 3
Theoretical and observed supraglacial pond omissions using the 2016 imagery set.

Sensor	Pixel area (m ²)	Reference pond area < one pixel (theoretical omissions) (%) of total	Observed pond area omission (%) of total	Reference pond number < one pixel (theoretical omission) (%) of total	Observed pond number omission (%) of total	Observed pond area net difference (%) ^b	Observed pond number net difference (%) ^b
PlanetScope ^a	9	< 1	–	< 1	–	–	–
RapidEye	25	< 1	7	< 1	48	–1	–2
Sentinel-2 _{NIR}	100	4	10	48	55	–1	–37
ASTER ^a	225	9	–	67	–	–	–
Sentinel-2 _{SWIR}	400	15	–	77	–	–	–
Landsat 8	900	26	34	87	88	–11	–86

^a PlanetScope (3 m spatial resolution) and ASTER (15 m spatial resolution) imagery were not used in the 2016 analysis, but are included for comparison.

^b Compared to the area and number of ponds in reference dataset when accounting for commissions and omissions.

6. Conclusion

We performed a quantitative analysis of the performance of fine- to medium-resolution satellite imagery products for classifying supraglacial ponds on debris-covered glaciers in the Everest region of Nepal. We investigated the relationship between calculated NDWI values and pixel water content using fine-resolution reference pond datasets for RapidEye, Sentinel-2 and Landsat 8 imagery. We then derived the optimum NDWI value for pond area classification on Khumbu Glacier, which was applied to and evaluated on seven other debris-covered glaciers.

NDWI values calculated using Sentinel-2 imagery showed the greatest spectral difference between water and surrounding debris cover, and a NDWI calculated using the NIR and green bands displayed the strongest relationship with pixel water content ($R^2 = 0.56$), followed by RapidEye NDWI ($R^2 = 0.45$). By optimising NDWI values using a reference pond dataset, RapidEye and Sentinel-2_{NIR} NDWI-Os correctly accounted for 99% of the 2016 reference dataset's total pond area, whereas the Landsat 8 NDWI-O accounted for only 89%. However, the apparent accuracy of Landsat 8 was a net result of large omissions and commissions and the classification accuracy was variable amongst individual glaciers. At the scale of individual ponds, comparisons between classified and reference dataset ponds had the highest correlations and lowest RMSE for RapidEye (424 m²) and Sentinel-2_{NIR} (446 m²), and the highest RMSE for Landsat 8 (2489 m²).

Our findings suggest that imagery ≤ 10 m resolution is well suited to supraglacial pond analysis on debris-covered glaciers where the role of individual ponds is important. NDWI-based semi-automated classification methods benefit from using a fine-resolution reference dataset to optimise the NDWI value used to classify ponds, and to quantify omissions and commissions in the classification. Therefore, our method of supraglacial pond classification can help develop a more detailed understanding of debris-covered glacier water storage and ponds' evolution towards glacial lake development, which require monitoring for emerging GLOF risks.

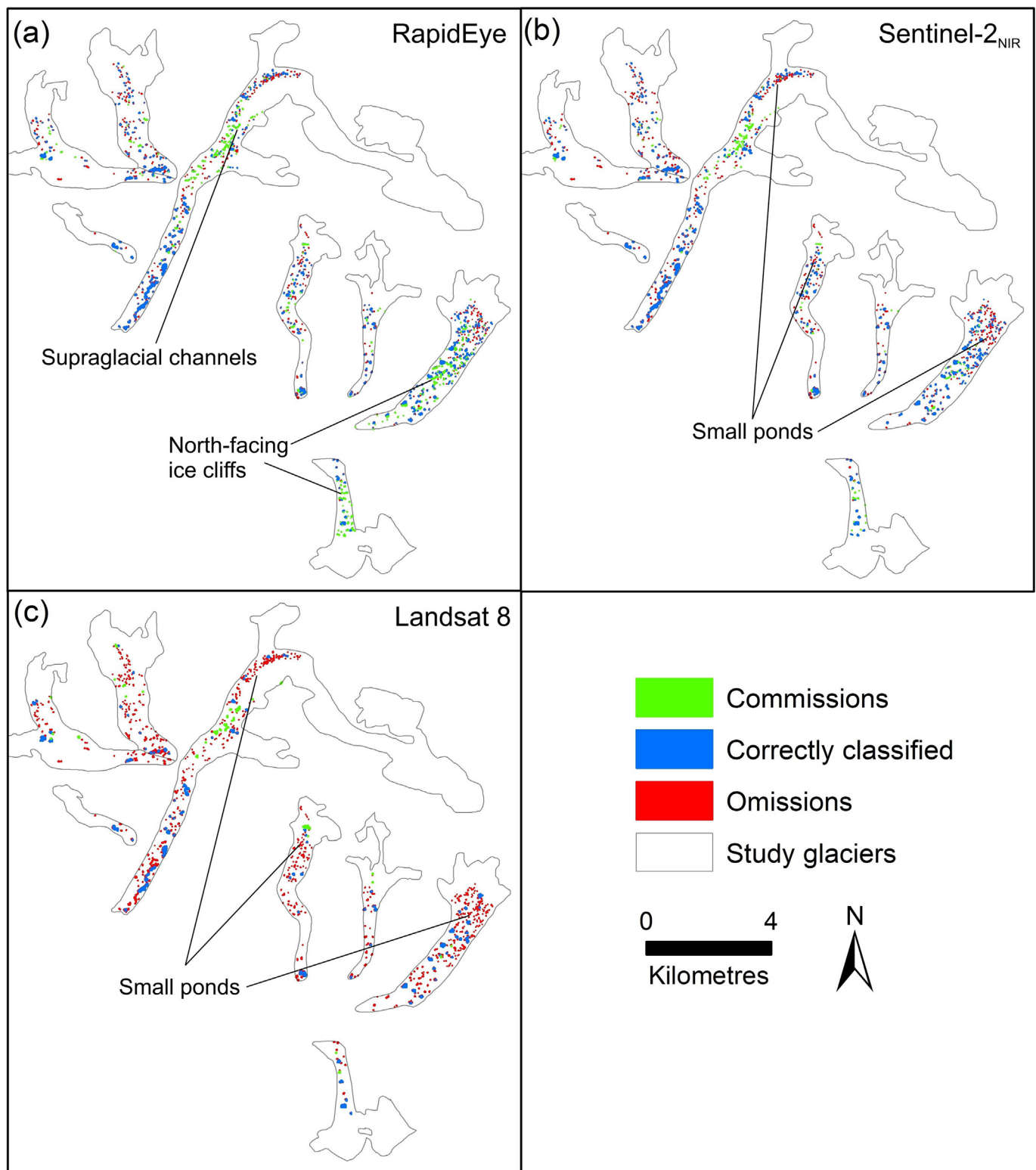


Fig. 7. Omissions and commissions of supraglacial ponds in 2016 for (a) RapidEye, (b) Sentinel-2_{NIR}, and (c) Landsat 8. Features causing the differences are highlighted. Glacier outlines are the same as Fig. 1. An enlarged version of this figure is available in Supplementary information.

Table 4

Sensitivity of reference dataset pond area delineation to selection of the NDWI value. Uncertainty values were derived from a plus or minus one-pixel perimeter buffer applied to the reference pond datasets.

	NDWI	NDWI-O (100% of true pond area)	NDWI-80 (80% of true pond area)	NDWI-120 (120% of true pond area)
2016	RapidEye	-0.29 ± 0.01	-0.33 ± 0.02	-0.27 ± 0.01
	Sentinel-2 _{NIR}	-0.19 ± 0.02	-0.23 ± 0.02	-0.15 ± 0.01
	Landsat 8	-0.19 ± 0.02	-0.23 ± 0.02	-0.15 ± 0.01
2017	RapidEye	-0.29 ± 0.01	-0.32 ± 0.01	-0.27 ± 0.01
	Sentinel-2 _{NIR}	-0.22 ± 0.08	-0.28 ± 0.08	-0.18 ± 0.08
	Landsat 8	-0.25 ± 0.10	-0.29 ± 0.12	-0.21 ± 0.08

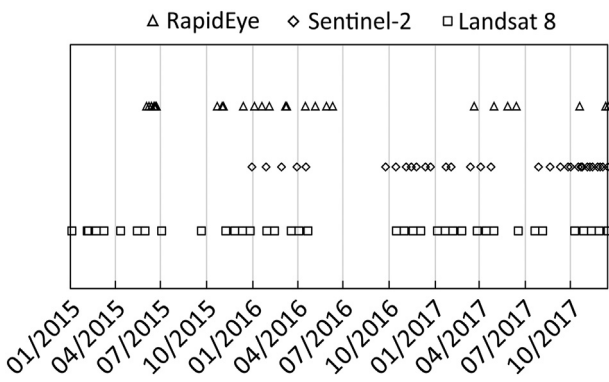


Fig. 8. Useable satellite images (low or no cloud) acquired over our study area 2015–2017.

Supplementary data to this article can be found online at <https://doi.org/10.1016/j.rse.2018.08.020>.

Acknowledgements

CSW acknowledges support from the School of Geography at the University of Leeds, the Mount Everest Foundation, the British Society for Geomorphology, the Royal Geographical Society (with IBG), the Petzl Foundation, water@leeds, NASA High Mountain Asia grant NNX16AQ62G, and NASA IDS grant 80NSSC18K0432. OK is a recipient of a NERC DTP PhD studentship (grant award NE/L002574/1). Pléiades satellite images were supplied by Airbus Defence and Space through a Category-1 agreement with the European Space Agency (ID Nr. 32600). Planet Labs are thanked for providing access to the archive of RapidEye and PlanetScope imagery through the Planet Application Program Interface: In Space for Life on Earth, San Francisco, CA. (<https://api.planet.com>). This study contains modified Copernicus Sentinel-2 data (2017), and NASA Land Processes Distributed Active Archive Center (LP DAAC) Products. The ASTER GDEM is a product of NASA and METI and we thank the European Space Agency and the United States Geological Survey for making these data accessible. We thank the RGI Consortium for providing access to glacier outlines. The Natural Environment Research Council Geophysical Equipment Facility is thanked for loaning Global Navigation Satellite Systems receivers and for technical assistance under loan numbers 1050, 1058, and 1065. We thank three anonymous reviewers for thorough comments that improved this study.

References

Alcántara, E., Barbosa, C., Stech, J., Novo, E., Shimabukuro, Y., 2009. Improving the spectral unmixing algorithm to map water turbidity distributions. *Environ. Model. Softw.* 24 (9), 1051–1061. <https://doi.org/10.1016/j.envsoft.2009.02.013>.

Benn, D.I., Bolch, T., Hands, K., Gulley, J., Luckman, A., Nicholson, L.I., Quincey, D., Thompson, S., Toumi, R., Wiseman, S., 2012. Response of debris-covered glaciers in the Mount Everest region to recent warming, and implications for outburst flood hazards. *Earth Sci. Rev.* 114 (1–2), 156–174. <https://doi.org/10.1016/j.earscirev.2012.03.008>.

Buri, P., Miles, E.S., Steiner, J.F., Immerzeel, W.W., Wagnon, P., Pellicciotti, F., 2016. A physically-based 3D-model of ice cliff evolution over debris-covered glaciers. *J. Geophys. Res. Earth Surf.* 2471–2493. <https://doi.org/10.1002/2016JF004039>.

Carrivick, J.L., Tweed, F.S., 2013. Proglacial lakes: character, behaviour and geological importance. *Quat. Sci. Rev.* 78, 34–52. <https://doi.org/10.1016/j.quascirev.2013.07.028>.

Chander, G., Haque, M.O., Sampath, A., Brunn, A., Trosset, G., Hoffmann, D., Roloff, S., Thiele, M., Anderson, C., 2013. Radiometric and geometric assessment of data from the RapidEye constellation of satellites. *Int. J. Remote Sens.* 34 (16), 5905–5925. <https://doi.org/10.1080/01431161.2013.798877>.

Cooley, S., Smith, L., Stepan, L., Mascaro, J., 2017. Tracking dynamic northern surface water changes with high-frequency Planet CubeSat imagery. *Remote Sens.* 9 (12), 1306. <https://doi.org/10.3390/rs9121306>.

Du, Z., Li, W., Zhou, D., Tian, L., Ling, F., Wang, H., Gui, Y., Sun, B., 2014. Analysis of Landsat-8 OLI imagery for land surface water mapping. *Remote Sens. Lett.* 5 (7), 672–681. <https://doi.org/10.1080/2150704X.2014.960606>.

Fawcett, T., 2006. An introduction to ROC analysis. *Pattern Recogn. Lett.* 27 (8), 861–874. <https://doi.org/10.1016/j.patrec.2005.10.010>.

Fujita, K., Sakai, A., Nuimura, T., Yamaguchi, S., Sharma, R.R., 2009. Recent changes in Imja Glacial Lake and its damming moraine in the Nepal Himalaya revealed by in situ surveys and multi-temporal ASTER imagery. *Environ. Res. Lett.* 4, 1–7. <https://doi.org/10.1088/1748-9326/4/4/045205>.

Gardelle, J., Arnaud, Y., Berthier, E., 2011. Contrasted evolution of glacial lakes along the Hindu Kush Himalaya mountain range between 1990 and 2009. *Glob. Planet. Chang.* 75 (1–2), 47–55. <https://doi.org/10.1016/j.gloplacha.2010.10.003>.

Huggel, C., Kääb, A., Haeblerli, W., Teyssie, P., Paul, F., 2002. Remote sensing based assessment of hazards from glacier lake outbursts: a case study in the Swiss Alps. *Can. Geotech. J.* 39 (2), 316–330. <https://doi.org/10.1139/t01-099>.

Immerzeel, W.W., Kraaijenbrink, P.D.A., Shea, J.M., Shrestha, A.B., Pellicciotti, F., Bierkens, M.F.P., de Jong, S.M., 2014. High-resolution monitoring of Himalayan glacier dynamics using unmanned aerial vehicles. *Remote Sens. Environ.* 150, 93–103. <https://doi.org/10.1016/j.rse.2014.04.025>.

Irvine-Fynn, T.D.L., Porter, P.R., Rowan, A.V., Quincey, D.J., Gibson, M.J., Bridge, J.W., Watson, C.S., Hubbard, A., Glasser, N.F., 2017. Supraglacial ponds regulate runoff from Himalayan debris-covered glaciers. *Geophys. Res. Lett.* 44 (23), 894–904. <https://doi.org/10.1002/2017GL075398>.

Ji, L., Zhang, L., Wylie, B., 2009. Analysis of dynamic thresholds for the normalized difference water index. *Photogramm. Eng. Remote. Sens.* 75, 1307–1317.

King, O., Quincey, D.J., Carrivick, J.L., Rowan, A.V., 2017. Spatial variability in mass loss of glaciers in the Everest region, central Himalayas, between 2000 and 2015. *Cryosphere* 11 (1), 407–426. <https://doi.org/10.5194/tc-11-407-2017>.

Kirkbride, M.P., 1993. The temporal significance of transitions from melting to calving termini at glaciers in the central Southern Alps of New Zealand. *The Holocene* 3 (3), 232–240. <https://doi.org/10.1177/095968369300300305>.

Kotchenova, S.Y., Vermote, E.F., 2007. Validation of a vector version of the 6S radiative transfer code for atmospheric correction of satellite data. Part II. Homogeneous Lambertian and anisotropic surfaces. *Appl. Opt.* 46 (20), 4455–4464. <https://doi.org/10.1364/AO.46.004455>.

Kotchenova, S.Y., Vermote, E.F., Matarrese, R., Klemm Jr., F.J., 2006. Validation of a vector version of the 6S radiative transfer code for atmospheric correction of satellite data. Part I: path radiance. *Appl. Opt.* 45 (26), 6762–6774. <https://doi.org/10.1364/AO.45.006762>.

Kraaijenbrink, P.D.A., Shea, J.M., Pellicciotti, F., de Jong, S.M., Immerzeel, W.W., 2016. Object-based analysis of unmanned aerial vehicle imagery to map and characterise surface features on a debris-covered glacier. *Remote Sens. Environ.* 186, 581–595. <https://doi.org/10.1016/j.rse.2016.09.013>.

Leeson, A.A., Shepherd, A., Sundal, A.V., Malin Johansson, A., Selmes, N., Briggs, K., Hogg, A.E., Fettweis, X., 2013. A comparison of supraglacial lake observations derived from MODIS imagery at the western margin of the Greenland ice sheet. *J. Glaciol.* 59 (218), 1179–1188. <https://doi.org/10.3189/2013JoG13J064>.

Li, W., Du, Z., Ling, F., Zhou, D., Wang, H., Gui, Y., Sun, B., Zhang, X., 2013. A comparison of land surface water mapping using the normalized difference water index from TM, ETM+ and ALI. *Remote Sens.* 5 (11), 5530–5549. <https://doi.org/10.3390/rs5115530>.

Liu, Q., Christoph, M., Shiyin, L., 2015. Distribution and interannual variability of supraglacial lakes on debris-covered glaciers in the Khan Tengri-Tumour Mountains, Central Asia. *Environ. Res. Lett.* 10 (1), 1–10. <https://doi.org/10.1088/1748-9326/10/1/014014>.

McFeeters, S.K., 1996. The use of the Normalized Difference Water Index (NDWI) in the

- delineation of open water features. *Int. J. Remote Sens.* 17 (7), 1425–1432. <https://doi.org/10.1080/01431169608948714>.
- Miles, E.S., Pellicciotti, F., Willis, I.C., Steiner, J.F., Buri, P., Arnold, N.S., 2016a. Refined energy-balance modelling of a supraglacial pond, Langtang Khola, Nepal. *Ann. Glaciol.* 57 (71), 29–40. <https://doi.org/10.3189/2016AoG71A421>.
- Miles, E.S., Willis, I.C., Arnold, N.S., Steiner, J., Pellicciotti, F., 2016b. Spatial, seasonal and interannual variability of supraglacial ponds in the Langtang Valley of Nepal, 1999–2013. *J. Glaciol.* 63 (237), 1–18. <https://doi.org/10.1017/jog.2016.120>.
- Miles, E.S., Steiner, J., Willis, I., Buri, P., Immerzeel, W.W., Chesnokova, A., Pellicciotti, F., 2017a. Pond dynamics and supraglacial-englacial connectivity on debris-covered Lirung Glacier, Nepal. *Front. Earth Sci.* 5 (69). <https://doi.org/10.3389/feart.2017.00069>.
- Miles, K.E., Willis, I.C., Benedek, C.L., Williamson, A.G., Tedesco, M., 2017b. Toward monitoring surface and Subsurface Lakes on the Greenland ice sheet using Sentinel-1 SAR and Landsat-8 OLI imagery. *Front. Earth Sci.* 5 (58). <https://doi.org/10.3389/feart.2017.00058>.
- Narama, C., Daiyrov, M., Tadono, T., Yamamoto, M., Kääb, A., Morita, R., Ukita, J., 2017. Seasonal drainage of supraglacial lakes on debris-covered glaciers in the Tien Shan Mountains, Central Asia. *Geomorphology* 286, 133–142. <https://doi.org/10.1016/j.geomorph.2017.03.002>.
- NASA Earth Observations, 2018. Aerosol Optical thickness (1 month - Terra/MODIS). http://neo.sci.gsfc.nasa.gov/view.php?datasetId=MODAL2_M_AER_OD.
- Nie, Y., Liu, Q., Liu, S., 2013. Glacial lake expansion in the Central Himalayas by Landsat images, 1990–2010. *PLoS ONE* 8 (12), 1–8. <https://doi.org/10.1371/journal.pone.0083973>.
- Planet Team, 2017. Planet Application Program Interface. Space for Life on Earth, San Francisco, CA. <https://api.planet.com>.
- Quincey, D.J., Richardson, S.D., Luckman, A., Lucas, R.M., Reynolds, J.M., Hambrey, M.J., Glasser, N.F., 2007. Early recognition of glacial lake hazards in the Himalaya using remote sensing datasets. *Glob. Planet. Chang.* 56 (1–2), 137–152. <https://doi.org/10.1016/j.gloplacha.2006.07.013>.
- Quincey, D.J., Luckman, A., Benn, D., 2009. Quantification of Everest region glacier velocities between 1992 and 2002, using satellite radar interferometry and feature tracking. *J. Glaciol.* 55 (192), 596–606. <https://doi.org/10.3189/002214309789470987>.
- Ragettli, S., Bolch, T., Pellicciotti, F., 2016. Heterogeneous glacier thinning patterns over the last 40 years in Langtang Himal, Nepal. *Cryosphere* 10 (5), 2075–2097. <https://doi.org/10.5194/tc-10-2075-2016>.
- Reynolds, J.M., 2000. On the formation of supraglacial lakes on debris-covered glaciers. In: Nakawo, M., Raymond, C.F., Fountain, A. (Eds.), *IAHS Publ.* 264 (Symposium at Seattle 2000 – Debris-covered Glaciers). IAHS Publishing, Seattle, Washington, USA, pp. 153–161.
- RGI Consortium, 2017. Randolph Glacier Inventory – A Dataset of Global Glacier Outlines: Version 6.0: Technical Report, Global Land Ice Measurements from Space. <https://doi.org/10.7265/N5-RGI-60>.
- Rohr, K., 2008. Characteristics and evolution of supraglacial ponds on debris-covered Tasman Glacier, New Zealand. *J. Glaciol.* 54 (188), 867–880. <https://doi.org/10.3189/002214308787779861>.
- Rounce, D., Watson, C., McKinney, D., 2017. Identification of hazard and risk for glacial lakes in the Nepal Himalaya using satellite imagery from 2000–2015. *Remote Sens.* 9 (7). <https://doi.org/10.3390/rs9070654>.
- Sakai, A., Nishimura, K., Kadota, T., Takeuchi, N., 2009. Onset of calving at supraglacial lakes on debris-covered glaciers of the Nepal Himalaya. *J. Glaciol.* 55 (193), 909–917. <https://doi.org/10.3189/002214309790152555>.
- Salerno, F., Thakuri, S.D., Agata, C., Smiraglia, C., Manfredi, E.C., Viviano, G., Tartari, G., 2012. Glacial lake distribution in the Mount Everest region: uncertainty of measurement and conditions of formation. *Glob. Planet. Chang.* 92–93, 30–39. <https://doi.org/10.1016/j.gloplacha.2012.04.001>.
- Salerno, F., Guyennon, N., Thakuri, S., Viviano, G., Romano, E., Vuillermoz, E., Cristofanelli, P., Stocchi, P., Agrillo, G., Ma, Y., Tartari, G., 2015. Weak precipitation, warm winters and springs impact glaciers of south slopes of Mt. Everest (central Himalaya) in the last 2 decades (1994–2013). *Cryosphere* 9 (3), 1229–1247. <https://doi.org/10.5194/tc-9-1229-2015>.
- Shrestha, A.B., Aryal, R., 2011. Climate change in Nepal and its impact on Himalayan glaciers. *Reg. Environ. Chang.* 11, 65–77. <https://doi.org/10.1007/s10113-010-0174-9>.
- Sundal, A.V., Shepherd, A., Nienow, P., Hanna, E., Palmer, S., Huybrechts, P., 2009. Evolution of supra-glacial lakes across the Greenland ice sheet. *Remote Sens. Environ.* 113 (10), 2164–2171. <https://doi.org/10.1016/j.rse.2009.05.018>.
- Thompson, S., Benn, D., Mertes, J., Luckman, A., 2016. Stagnation and mass loss on a Himalayan debris-covered glacier: processes, patterns and rates. *J. Glaciol.* 62 (233), 467–485. <https://doi.org/10.1017/jog.2016.37>.
- Vermote, E.F., Tanre, D., Deuze, J.L., Herman, M., Morcette, J.J., 1997. Second Simulation of the Satellite Signal in the Solar Spectrum, 6S: an overview. *IEEE Trans. Geosci. Remote Sens.* 35 (3), 675–686. <https://doi.org/10.1109/36.581987>.
- Vuolo, F., Zóttak, M., Pipitone, C., Zappa, L., Wennig, H., Immitzer, M., Weiss, M., Baret, F., Atzberger, C., 2016. Data service platform for Sentinel-2 surface reflectance and value-added products: system use and examples. *Remote Sens.* 8 (11). <https://doi.org/10.3390/rs8110938>.
- Watson, C.S., King, O., 2018. Everest's thinning glaciers: implications for tourism and mountaineering. *Geol. Today* 34 (1), 18–25. <https://doi.org/10.1111/gto.12215>.
- Watson, C.S., Quincey, D.J., Carrivick, J.L., Smith, M.W., 2016. The dynamics of supraglacial ponds in the Everest region, central Himalaya. *Glob. Planet. Chang.* 142, 14–27. <https://doi.org/10.1016/j.gloplacha.2016.04.008>.
- Watson, C.S., Quincey, D.J., Carrivick, J.L., Smith, M.W., 2017a. Ice cliff dynamics in the Everest region of the Central Himalaya. *Geomorphology* 278, 238–251. <https://doi.org/10.1016/j.geomorph.2016.11.017>.
- Watson, C.S., Quincey, D.J., Carrivick, J.L., Smith, M.W., Rowan, A.V., Richardson, R., 2017b. Heterogeneous water storage and thermal regime of supraglacial ponds on debris-covered glaciers. *Earth Surf. Process. Landf.* 229–241. <https://doi.org/10.1002/esp.4236>.
- Watson, C.S., Quincey, D.J., Smith, M.W., Carrivick, J.L., Rowan, A.V., James, M., 2017c. Quantifying ice cliff evolution with multi-temporal point clouds on the debris-covered Khumbu Glacier, Nepal. *J. Glaciol.* 823–837. <https://doi.org/10.1017/jog.2017.47>.
- Williamson, A.G., Arnold, N.S., Banwell, A.F., Willis, I.C., 2017. A Fully Automated Supraglacial lake area and volume Tracking (“FAST”) algorithm: development and application using MODIS imagery of West Greenland. *Remote Sens. Environ.* 196, 113–133. <https://doi.org/10.1016/j.rse.2017.04.032>.
- Worni, R., Huggel, C., Clague, J.J., Schaub, Y., Stoffel, M., 2014. Coupling glacial lake impact, dam breach, and flood processes: a modeling perspective. *Geomorphology* 224, 161–176. <https://doi.org/10.1016/j.geomorph.2014.06.031>.